3.1 Introduction

In the current scenario, energy generation, conversions, and storage have become a global concern due to the continuous rise in the gap between energy demand and supply associated with the rapid growth and industrialization of the world. For the past three decades, lithium-ion battery (LIB) technologies have dominated the portable electronic world and are envisaged as a potential candidate for power supply in electric and hybrid electric vehicles due to their lightweight and high energy density(Etacheri et al., 2011). Due to the limited availability of lithium and its uneven geographical distribution associated with high cost(Bruce et al., 2008; Goodenough & Park, 2013), a concern arises about whether lithium-ion can alone satisfy the rising global needs for small and large energy storage girds. The increasing global energy demands force the systematic development of alternative rechargeable energy storage options such as sodium-ion batteries (NIB)(Sagar Mitra et al. 2021, M. Yang et al., 2022), potassium-ion batteries (PIB) (Eftekhari, 2004), magnesium ion batteries (MIB) (Huie et al., 2015), etc. Among those possible next-generation batteries, NIB can be considered as the best potential alternative to LIBs for the following advantages a) sodium element is widely available on the earth/sea and very cheap(K. Zhang et al., 2015), b) exhibits very similar chemistry to lithium(Lu et al., 2010), c) second lightest and smallest alkali metal after Li. Moreover, sodium-ion batteries have excellent electrochemical features in terms of good reversibility, coulombic efficiency, and high specific discharge capacity. Hence, these advantages, in addition to the appreciable redox potential with lithium (<0.3 V with respect to Li), make NIBs an appropriate choice for an alternative rechargeable battery system. However, there are a few challenges in the practical implementation of NIBs owing to the following reasons; a) larger radius of Na ion (0.98 Å) as compared to that of lithium-ion (0.69 Å), b) sluggish diffusion coefficient of Na ion,(He et al.,

2015) c) poor cyclability and rate capability(Klein et al., 2013), d) stronger Na-Na coulombic interactions that hinder sodium-ion insertion/de-insertion in the host structure, (Komaba et al., 2012) e) lower Madelung energies giving rise to low cell voltages and f) heavier atomic weight than lithium (23 g/mol vs 7 g/mol). In addition to the inherent thermodynamic disadvantages, NIBs have to overcome multiple kinetic problems such as fast capacity decay, poor cyclability and lower solubility in the solid state, low-rate capacities, low energy density, low columbic efficiency, and rate capability.

Several layered oxide host cathode materials for NIB, such as Na_xMO_2 (M=Co, Fe, Mn, V, Cr, etc.), transition metal fluorides ($NaMF_3$, where M= Fe, Mn, Ni, and V), pyrophosphate, and organic compounds have been investigated thoroughly(Delmas et al., 1981a; C. Deng et al., 2016; Guo et al., 2015; Gupta et al., 2013a) for development of NIBs. However, these structures have few hindrances in practical implications, such as narrow ion diffusion tunnels, irreversible phase transition after Na intercalation, poor structural stability, low power density, and poor long-term cycling performance. Hexagonal $Na_{1+3x}\ Zr_2(P_{1-x}Si_xO_4)_3$ was identified as a fast Na^+ conductor over the range $0 < x < 1$; the best Na^+ Conductor ($x = 2/3$) was called NASICON. The general formula for NASICON-type structure materials is $Na_XMM'(XO_4)_3$ (where M = V, Ti, Fe, Nb, and X= P, Si or S, x = 0-4). With the incorporation of active redox couples, Sodium superionic conductor (NASICON) with its open three-dimensional framework and associated structural (frameworks) stability can be a promising host structure for NIBs (Qiu et al., 2019; C. Wu et al., 2015). It possesses the following advantage over other structures such as high sodium-ion conductivity, negligible structural/volume changes, excellent thermal stability, and chemical flexibility. The structure is formed by corner-shared MO_6 octahedral and interconnecting XO_4 tetrahedral groups, which provide

three-dimensional sodium-ion diffusion channels(Sawicki & Shaw, 2015). In this paper, I report on the synthesis, characterizations, and investigation of the reversible in/desertion sodium-ion into $Na_3Fe_2(SO_4)_2PO_4$ as a cathode for NIBs. With the utilization of inductive effects in the polyanion framework system (Manthiram & Goodenough, 1989; Padhi, Nanjundaswamy, Masquelier, et al., 1997; Wei et al., 2016), the Fe^{3+}/Fe^{2+} redox potential was further enhanced by replacing the PO_4^{3-} units with more ionic sulphate units thereby utilizing higher electronegativity. So capacity and stability is a major concern for sodium-ion battery regarding stability and capacity; recent research has been done to improve the cathode performance e.g., doping with Ca^{2+} (Li, Gu, et al., 2021), modification with rGO (Li, Hou, et al., 2021), and all climate stable cathode (Gu et al., 2021) for high capacity sodium-ion battery.

3.2 Experimental Section

A low-cost and low-temperature synthesis route was used to synthesize $Na_3Fe_2PO_4(SO_4)_2$. 0.02 M $(NH_4)_2Fe(SO_4)_2$, 0.01 M NaH_2PO_4 were dissolved in 100 ml of water under continuous stirring at 120 °C on a hot stirring plate. 0.01 M Na_2CO_3 Sodium carbonate was added to the above mixture leading to a spontaneous evolution of CO_2 gas and the formation of a water-insoluble compound. Water was removed by drying at 100 °C, and yellow-colored powder was obtained. The resulting yellow powder was ground and transferred into an alumina crucible to be sintered at 500 °C for 12 hours (at a ramp rate of 2 °C per minute). As sulphate ion decomposes to SO_2 gas above 600 ^oC, I sintered the sample at 500 ^oC to avoid any loss of sulphate ions. The sample was cooled naturally till it reached room temperature (25 °C), and yellowish green crystalline $Na_3Fe_2PO_4(SO_4)_2$ material was obtained. The phase purity and structure stability of the prepared powders were confirmed by the powder X-ray

diffraction (XRD) analysis carried out with a Rigaku miniflex Diffractometer equipped with a Cu Kα source (1λ = 1.54056 Å (voltage 40 kV, current 30 mA, 2 Θ – 10 to 0°). Rietveld refinement of the XRD pattern was performed using the fullproof program taking $Na_3Cr_2(PO4)_3$ structure in $R\bar{3}c$ space group as the model structure. The microstructure and elemental mapping of the powders were analyzed with Zeiss attached with an EDS microscope operating at 20 kV. The Thermogravimetric analysis (TGA) was carried out using TG/DSC analyzer in the nitrogen atmosphere from room temperature to 800 °C at a heating rate of 10 °C/min.

3.3 Cell Assembling

Electrochemical analyses of cathode material were carried out by mixing active material (NFPS) and conducting carbon in the ratio of 7: 3 by weight. Thus, resulting cathode powders were made into Swagelok-type cells using sodium metal as both counter and reference electrodes. A porous glass microfiber filter paper (GF/D, Whatman Int. Ltd.) was used as a separator, and the electrolyte used was 1.0 M $NaPF_6$ in ethylene carbonate (EC)/ Propylene carbonate (PC) (1:1 v/v%). Cell assembly was carried out in an argon (99.999%) filled glove box (MBRAUN, Germany) where the H_2O and O_2 concentrations were maintained to ≤ 1 ppm while active mass loading of 4 - 5 mg per cell. The cyclic voltammetry and galvanostatic charge–discharge cycling tests of the cells were carried at different current rates within the voltage window of 1.5 - 4.2 V. Electrochemical impedance studies were performed over a frequency range from 400 kHz to 10 mHz with a bias voltage 20 mV applied vs. Na^0/Na^+. All the electrochemical tests were carried out using VMP3Z (Bio-logic) multichannel potentiostat/galvanostat workstations under ambient conditions.

3.4 Results and Discussion

3.4.1 Structural Analysis

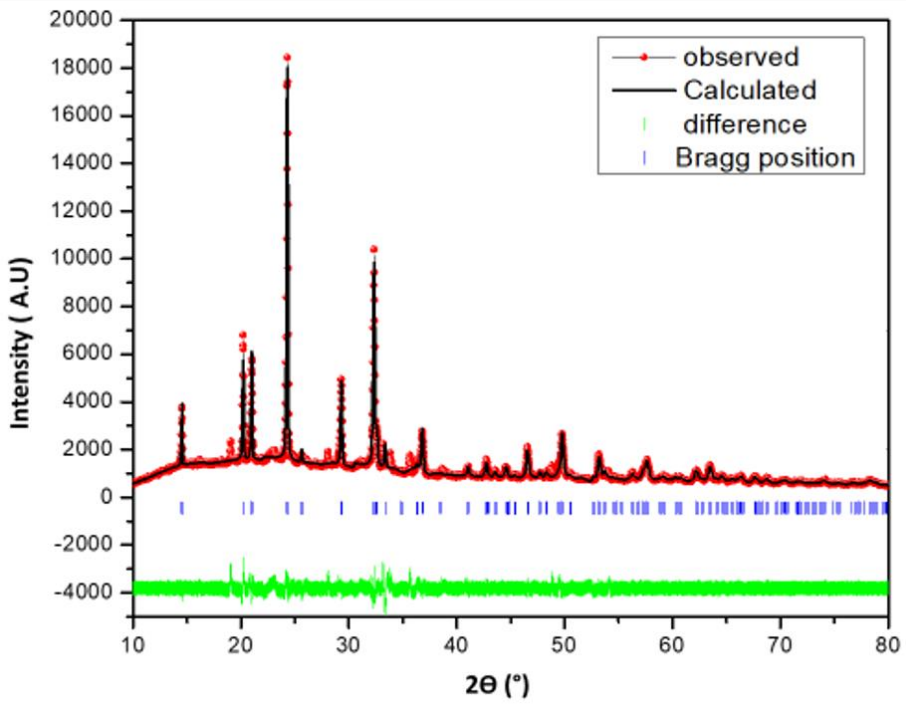

Figure 3.1 Rietveld refined *PXRD* profile of $Na_3Fe_2(SO_4)_2PO_4$.

Figure 3.1 shows the Rietveld refined XRD pattern of the $Na_3Fe_2PO_4(SO_4)_2$; the calculated and measured diffraction intensities match well, with little higher R values (R_{bragg} = 1.77412%, R_f =1.7750 % and c^2 =5.47%). The structural refinement confirms that the two different (XO_4) units bridging randomly the two octahedra of the $M_2(XO_4)_3$ molecular units; the (XO_4) units of these units corner share to build the host framework structure.

SEM images, Figure 3.2(a), (b), and (c) show the formation of agglomerated flakes as a layer on layers structure. The EDS image of Figure 3.2(d) confirms the composition of the sample to its chemical formula. Elemental mapping (Figure 3.3) shows the homogeneous distribution of the elements present in the sample.

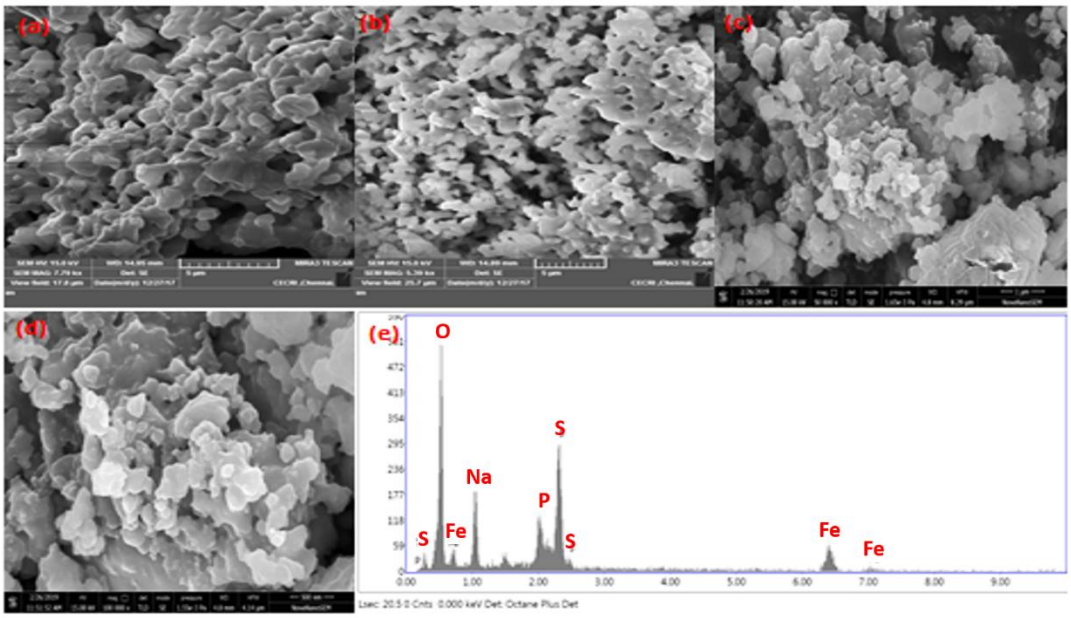

Figure 3.2 (**a-c**) SEM images and (e) EDS of as prepared $NaFe_2(SO_4)_2PO_4$ and (**d**) SEM image of $NaFe_2(SO_4)_2PO_4$ electrode.

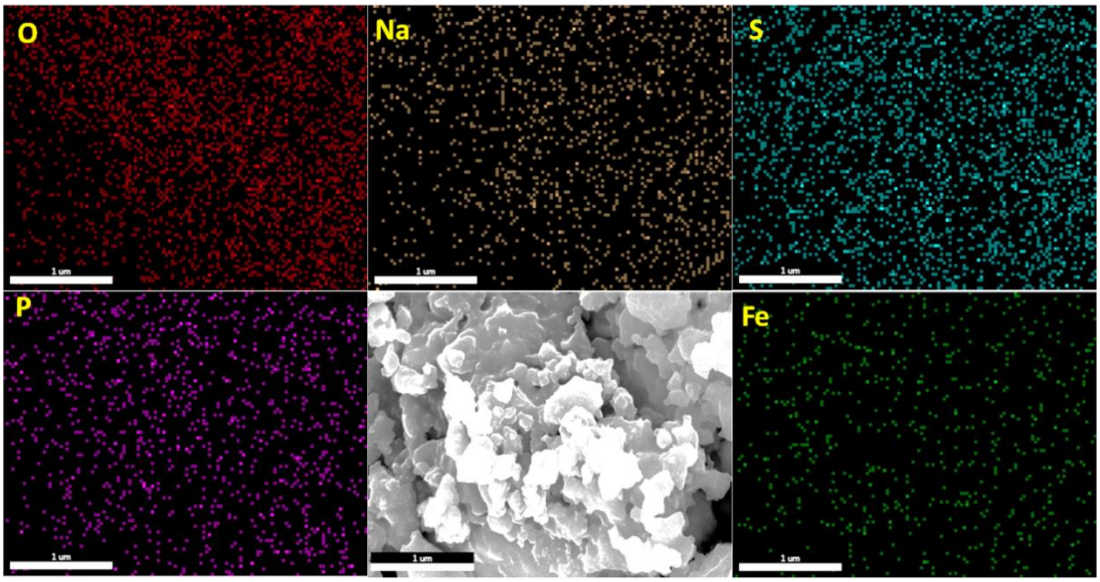

Figure 3.3 Elemental Mapping of NFSP electrodes

Following this, the material stability was studied by thermogravimetric analysis (TGA). Although sulphate-containing compounds are inclined to decompose after heating, the $Na_3Fe_2PO_4(SO_4)_2$ compound was observed to be steady until 600 ºC, thereafter, it begins deteriorating to discharge SO_x gases (Figure 3.4). The net weight reduction is restricted to

just 12.5 wt% until 700 ºC. It offers phenomenal thermal stability compared to $Na_{2+2x}Fe_{2-x}(SO_4)_3$, where the beginning of deterioration begins at ~ 450 ºC prompting critical weight reduction of more than 30 wt%. (Dwibedi et al., 2015).

Table 3.1 Chemical composition of NFSP

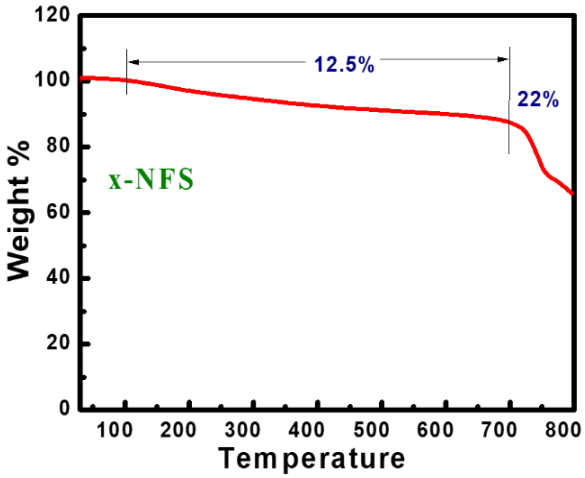

S.No	Element	Observed weight %	Theoretical weight %	K ration
1	O	38.76	41.05	0.1917
2	Na	14.67	14.74	0.0595
3	P	7.85	6.62	0.0632
4	S	17.5	13.71	0.1463
5	Fe	21.21	23.88	0.1834

Figure 3.4 TGA of NFSP electrode

Before cell assembling the electrode, the material is dried in an argon atmosphere for 12 hours at 120ºC to avoid any moisture content it left out in the material so that it could not impact the cell performance. Thus, the removal of moisture content and determination of functional group IR absorption spectra for NFSP is performed, as shown in figure 3.5. Small O-H stretching at 3000 is due to a very small amount of moisture content, S=O asymmetric and symmetric stretching vibration appear at 1097 and 1041, respectively. also, P-O asymmetric and symmetric stretching vibration appears at 986cm^{-1} and 960 $cm^{-1,}$ respectively while bending vibration of O-P-O and O-S-O comes in the range of 500-750cm^{-1}.(Ramaswamy et al., 2010a; Y. Shen et al., 2007; X. Zhao et al., 2020).

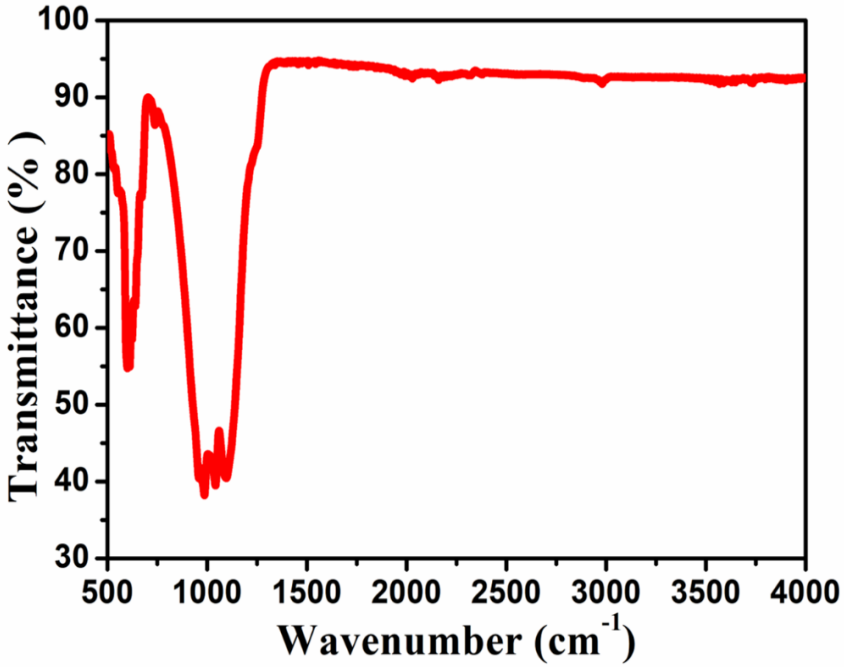

Figure 3.5 FTIR spectra of $Na_3Fe_2(SO_4)_2PO_4$.

3.4.2 Electrochemical Analysis

Cyclic voltammetry was performed to investigate the reversible redox process of the electrode material. Figure 3.6 (a) shows the cyclic voltammogram of five initial cycles within the voltage range of 1.5 – 4.2 V vs. Na/Na^+ at a 0.2 mV s^{-1} scan rate. During the first cathodic scan (Na^+ insertion), the peak is cantered at around 2.48 V, while in the anodic scan (Na^+ extraction), it is observed at 3.08 V. the Second cycle onwards, the peaks are shifted slightly to the higher potential and a decrease in the cathodic peak currents is observed. CV profiles depict that the $Na_3Fe_2PO_4(SO_4)_2$ is a 3V sodium insertion electrode with corresponding active Fe^{3+}/Fe^{2+} redox couple and cell reactions are given below

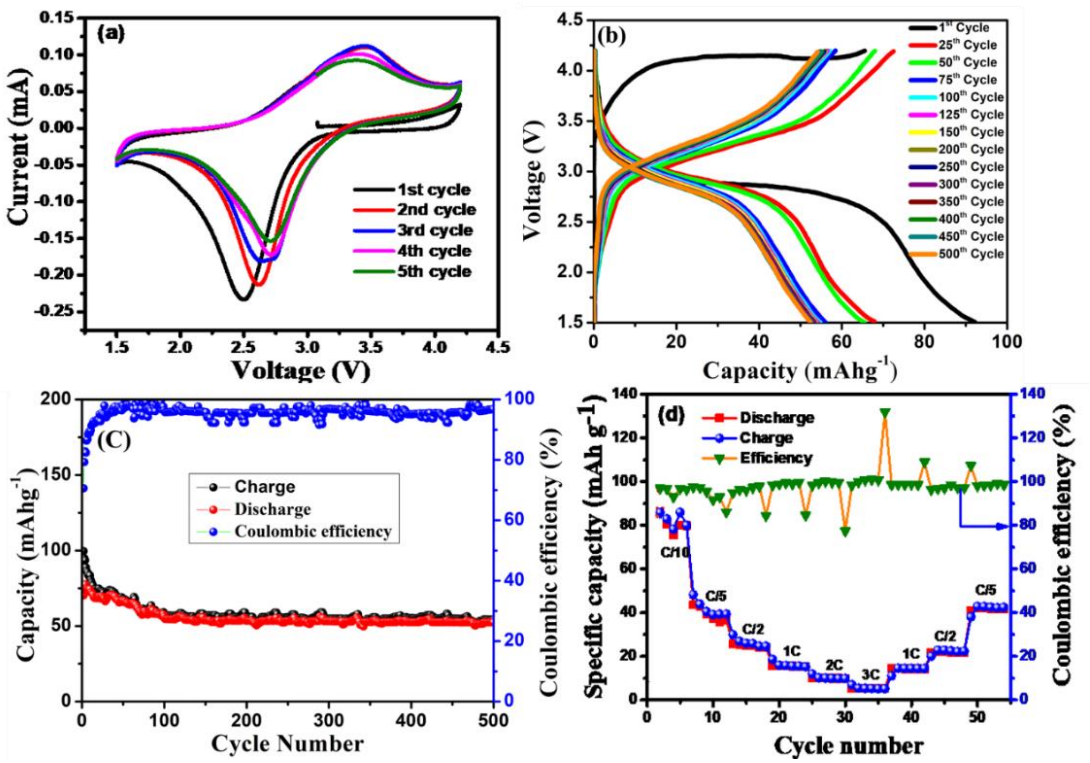

Figure 3.6 Electrochemical analysis of NFSP : (a) Cyclic voltammogram of initial five cycles within the voltage range 1.5 – 4.2 V at a scan rate 0.2 mV s^{-1} (b) selected charge-discharge cycling profiles (1^{st}, 25^{th}, 50^{th}, 75^{th}, and 100^{th}, 125^{th}, 150^{th}, 200^{th}, 250^{th}, 300^{th}, 350^{th}, 400^{th}, 450^{th}, 500^{th}) of NFSP at C/10 current rate (c) capacity retention and coulombic efficiency plot as a function of cycle number of NFSP for 500 cycles at C/10 (d) rate performance analysis of NFSP with a stepwise increase in current rates (C/10, C/5, C/2, 1C, 2C, and 3C)

$$Na_3Fe^{2+}{}_2(SO_4)_2PO_4 \underset{\text{Discharge}}{\overset{\text{Charge}}{\rightleftharpoons}} Na_{3-X}Fe^{3+}{}_2(SO_4)_2PO_4 + xNa + xe^- \quad \text{Eq. 3.1}$$

However, the cycling profiles are smooth and $I_p^a - I_P^C$ remains almost the same indicating reversible electrochemical activity. Figure 3.6 (b) shows the selected galvanostatic charge-discharge profiles (1^{st}, 25^{th}, 50^{th}, 75^{th}, and 100^{th}, 125^{th}, 150^{th}, 200^{th}, 250^{th}, 300^{th}, 350^{th}, 400^{th}, 450^{th}, 500^{th}) of the $Na_3Fe_2PO_4(SO_4)_2$/Na half-cell at a current

rate of C/10 (~12 mA g^{-1}). During the first charge, only 0.5 moles (28 mAh g^{-1}) of sodium could be de-intercalated from the $Na_3Fe_2PO_4(SO_4)_2$, whereas 1.6 moles of sodium could be intercalated (92 mAh g^{-1}) during the discharge. However, subsequent cycling profiles exhibit enhanced coulombic efficiencies and stable specific capacity (57 mAh g^{-1} and ~1 moles of reversible Na) up to 500 cycles. Both CV and cycling data reveal the sluggish sodium kinetics due to the insulating nature of $Na_3Fe_2PO_4(SO_4)_2$ as a cathode material as can be seen from Figure 3.6 (c); after a few cycles the charge-discharge capacities stabilized and resulted in high coulombic efficiencies. The $Na_3Fe_2PO_4(SO_4)_2$/Na half-cell exhibits a stable discharge capacity of 70 mAh g^{-1} up to 40 cycles, which is about 93% of its initial capacity. The capacity is stabilized at 57 mAh g^{-1} after 500 cycles. Figure 3.6 (d) shows the rate performance of the $Na_3Fe_2PO_4(SO_4)_2$/Na half-cell cycled at C/10, C/5, C/2, 1C, 2C, and 3C rate and showed discharge capacities of 80, 40, 25, 15, 10, and 7 mAh g^{-1} respectively. Insulating $Na_3Fe_2PO_4(SO_4)_2$ samples did not perform well at a higher current rate. From these electrochemical results, I believe that nanoengineering of the material could improve sodium-ion storage and can ensure high-rate performance. Figure 3.6 (e) shows the electrochemical impedance spectra (EIS) of the $Na_3Fe_2PO_4(SO_4)_2$ half cells. The Nyquist plots were fitted using an equivalent circuit consisting of uncompensated solution resistance of the electrolyte (R1) and the two semi-circles at the medium-high and low frequencies are due to the resistance offered by the solid electrolyte interface (R2) and charge transfer resistance of the $Na_3Fe_2PO_4(SO_4)_2$/Na half-cell (R3) respectively. Similarly, a sloppy line in the low-frequency range is related to Warburg impedance (W) correspond to the sodium-ion diffusion into the bulk phase. The impedance plot before and after 100 cycles remains almost unchanged confirming the stability and robustness of the $Na_3Fe_2PO_4(SO_4)_2$ in the NASICON structure

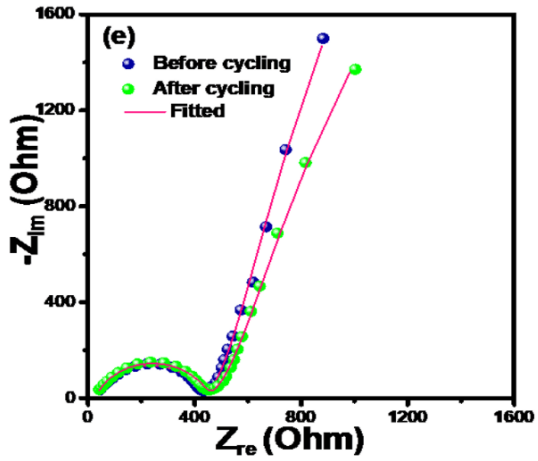

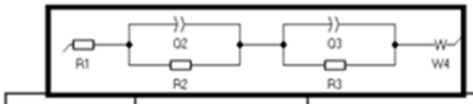

Parameter	Before cycling (Ω)	After cycling (Ω)
R1	26.4	25.41
R2	409.3	426.9
R3	9.938	5.847

Fig 3.6 (e) electrochemical impedance spectra (EIS) of as prepared and after completion of 100 charge-discharge cycles of NFSP and its equivalent circuit.

Table 3.2 Specific capacity profile of earlier reported NASICON framework cathode materials for sodium-ion battery

Material	C rate	Anode	Voltage	Capacity	Reference
$NaFe(SO_4)_2$	C/10	Na	3.0V	78 mAh/g	[(Singh et al., 2015a)]
$NaFe_{0.8}Cr_{0.2}(SO_4)_2$	C/10	Na	3.0V	58 mAh/g	[(Nisar et al., 2018a)]
$NaTi_2(PO_4)_3$	C/5	Na	2.0V	38 mAh/g	[(M. Wu et al., 2019)]
$Na_3Cr_2(PO_4)_3$	C/20	Na	4.5V	40 mAh/g	[(Kawai et al., 2019)]
$Na_3Fe_2(SO_4)_2PO_4$	C/10	Na	3.0V	70 mAh/g	Current work

3.5 Concluding Remark

- first time synthesis of NASICON framework structure $Na_3Fe_2PO_4(SO4)_2$ by a low-temperature process.
- Rhombohedral structured $Na_3Fe_2PO_4(SO_4)_2$ materials space group of R3/c as cathode material in NIBs.
- Structure confirmed by XRD studies and crystal structure refined using Rietveld refinement.
- Agglomerated flake morphology.
- Sulphate and Phosphate group presence confirm by FTIR spectroscopy.
- High Thermal stability up to 450^oC material application in a wide temperature range.
- Very high cyclic stability and reversible specific discharge capacity of ~75 $mAhg^{-1}$ at the current rate of 0.1 C, with a flat voltage plateau located at about 3.05 V.
- Single-phase $Na_3Fe_2PO_4(SO_4)_2$ de-intercalation of Na-ions at an average voltage of 3.05 V.
- No electrolyte or electrode degradation on cyclic charge-discharge up to 3.05V vs. Na.
- The stability of the electrode upon cyclic charge-discharge as the impedance of material before and after cycling is nearly the same.
- Smooth intercalation and deintercalation of sodium into the structure as coulombic efficiency reaches ~100%
- Once the bottleneck of relatively low specific discharge capacity is broken using nanoengineering, the low cost and environmental friendliness of

$Na_3Fe_2PO_4(SO_4)_2$ might have extensive application in energy storage systems in the form of NIBs.

- Further high potential window transition metal redox tuning can improve the overall Power density of NIB.